Sensors and Actuators A 184 (2012) 149–159

Contents lists available at SciVerse ScienceDirect

Sensors and Actuators A: Physical

journal homepage: www.elsevier.com/locate/sna

Investigation of piezoelectric driven MEMS mirrors based on single and double S-shaped PZT actuator for 2-D scanning applications

Kah How Koh[a], Takeshi Kobayashi[b], Chengkuo Lee[a,*]

[a] Department of Electrical & Computer Engineering, National University of Singapore, 4 Engineering Drive 3, Singapore 117576
[b] National Institute of Advanced Industrial Science and Technology (AIST), 1-2-1 Namiki, Tsukuba, Ibaraki 305-8564, Japan

ARTICLE INFO

Article history:
Received 13 February 2012
Received in revised form 19 June 2012
Accepted 19 June 2012
Available online 4 July 2012

Keywords:
Microelectromechanical systems (MEMS)
Optical MEMS
Piezoelectric actuator
PZT
Micromirror

ABSTRACT

A silicon micromirror driven by piezoelectric $Pb(Zr,Ti)O_3$ cantilever actuator has been demonstrated for 2-D scanning applications. Two different PZT actuator designs have been fabricated and characterized to investigate the effects of the dimensions and number of S-shaped PZT cantilever actuator folds on the 2-D scanning performances of the micromirror. Three modes of operation have also been investigated for both devices. Device A, which is driven by single S-shaped PZT cantilever actuator, performs better in both dc and ac laser scanning compared to device B, which is driven by double S-shaped PZT actuator. At 10 V_{dc}, static ODA of 4.6° and 3.3° are obtained for devices A and B respectively. In the ac actuation regime, device A achieved ±9.0° at resonant frequency of 27 Hz, 1 V_{pp} while device B achieved ±7.2° at 20 Hz, 1 V_{pp} for bending mode. In torsional mode, dynamic ODA peaks of ±1.8° and ±1.2° are observed at 70 Hz and 156 Hz for devices A and B respectively. Lissajous scan patterns for both devices have been successfully demonstrated by superimposing two ac sinusoidal signals of different frequencies into one signal to be used to actuate the mirror.

1. Introduction

Micromirrors realized by microelectromechanical systems (MEMS) technology have been widely used in numerous important optoelectronic applications such as optical communications [1–4], microspectroscopy [5–7], optical coherence tomography [8–11] and display [12–15]. MEMS and optics make a perfect match as MEMS devices have dimensions and actuation distances comparable to the wavelength of light. Besides using MEMS mirror which are reflective-type devices, diffractive-type in the form of gratings [16,17] and steering-type in the form of lens [18–20] have also been reported for scanning purposes. In recent years, optical MEMS devices have also formed a circle of growing interest with the development of handheld pico-projectors based on scanning mirror technology [21].

One of the key factors that have contributed to the remarkable MEMS commercial success is the development of Si-based micromachining technology and CMOS MEMS [22]. The integration of micromechanical parts and CMOS circuits have facilitated mass production of MEMS devices in CMOS foundries due to their high production yield, low fabrication cost etc. However, limited material selection in CMOS MEMS and CMOS compatible processes restrict the Si-based actuators to be mainly electrostatic or electrothermal [23–25]. Actuators deploying piezoelectric PZT ($PbZr_xTi_{1-x}O_3$) films are also attractive alternatives to Si-based actuators because of its potential to offer higher output force at lower voltage compared to the other actuators [26–29]. In a one-dimensional (1-D) resonant torsional micromirror based on 0.5 μm PZT thin film actuation, Filhol et al. achieved a total optical deflection angle (ODA), i.e. 4θ, of 78° at less than 1 V_{pp} in vacuum condition [30]. Besides 1-D resonant micromirror, two-dimensional (2-D) micromirror driven by double layered PZT actuators has also been developed by Tsaur et al. to yield larger bending force with lower actuation voltage [31]. In addition, Yasuda et al. reported a large elliptical 2-D micromirror driven by two orthogonal pairs of 3 μm PZT thin film ring actuators in a double-gimbal structure design [32]. In 2006, they demonstrated a new design where multiple meandering PZT actuators were adopted in both inner and outer frames so as to accumulate angular displacement and generate larger static deflection angle [33]. Recently, Zhu et al. demonstrated a tip-tilt-piston micromirror driven by four sets of piezoelectric unimorph PZT actuators, in which an optical scan range of 5° was obtained at 2 V_{pp} during resonance [34].

Besides the difference in actuation mechanisms, a wide variety of designs for 2-D scanning mirror have also been reported in the literature, with most of them deploying either the two frames or/and orthogonally arranged multi-actuators designs for 2-D actuation [31–40]. In addition, superimposition of ac currents corresponding to the frequencies of slow and fast scanning axis on the external

* Corresponding author. Tel.: +65 6516 5865; fax: +65 6779 1103.
E-mail address: elelc@nus.edu.sg (C. Lee).

0924-4247/$ – see front matter © 2012 Elsevier B.V. All rights reserved.
http://dx.doi.org/10.1016/j.sna.2012.06.018

electro-coil to illicit 2-D scanning have also been widely reported in electromagnetic actuated micromirror [13,38–42]. However, such electromagnetic actuated 2-D scanning mirrors require the presence of either an external permanent magnet or electromagnetic coil, resulting in bulky packaging.

On the other hand, two superimposed ac excitation biases, which have been performed on resistive type electromagnetic coils, are rarely examined on capacitive type piezoelectric actuator. Moreover, there are still limited research attempts on simple MEMS mirror design that utilizes only one or a set of actuators to achieve 2-D scanning. As a result, our motivation is to explore novel 2-D actuation mechanisms based on one or a set of piezoelectric actuators. In our previous research attempts, we have designed micromirrors driven by a 1×10 array of parallel arranged PZT cantilever actuators and demonstrated them for 2-D MEMS mirror scanning applications [43,44]. In our most recent work, we have also reported the development work of a 2-D MEMS scanning mirror actuated by a single meandering S-shaped PZT cantilever [45] and demonstrated the advantages of our new design over a straight beam design or those works we endeavored previously in Refs. [43,44]. As such, this research attempt aims to be an extended investigation on the effect of the meandering PZT cantilever actuator design on the actuation performance of the micromirror.

2. Design and modeling

A schematic diagram of the 2-D MEMS scanning mirror studied in this paper is shown in Fig. 1(a). The packaged device consists of a piezoelectric PZT S-shaped cantilever actuator driving and supporting a rectangular mirror plate simultaneously. The cross-section of the cantilever actuator consists of Pt/Ti (0.2 μm) top and bottom electrodes sandwiching a PZT thin film (2.5 μm), with a Si device layer (5 μm) providing mechanical strength to the actuator. The mirror plate is made up mainly of Si handle layer of 400 μm thick, hence maintaining the rigidity and preventing dynamic mirror deformation. There are only two bond pads for the device and are electrically connected to the top and bottom electrodes respectively. An elevating chip is placed beneath the mirror device so that the mirror plate has room for movement when driven by the PZT cantilever actuator. The mirror has six degrees of freedom and is designed to operate in 3 modes: bending, torsional and mixed. In bending mode, the mirror translates out of plane and rotates about the *x*-axis, while in torsional mode, the mirror twists and rotates about the *y*-axis.

Two actuator designs are developed in this research attempt to investigate the effect of the PZT cantilever actuator on the actuation performance of the mirror. As shown from the layout drawing in Fig. 1(b), the mirror plate for device A is driven by a single S-shaped PZT cantilever actuator with longitudinal (*y*-direction) and transverse (*x*-direction) lengths of 1.6 mm and 1.8 mm respectively. The layout drawing for device B is illustrated in Fig. 1(c), where the mirror plate is driven by a double S-shaped PZT cantilever actuator with longitudinal and transverse lengths of 1.8 mm and 1.7 mm respectively. The dimensions of the whole chip and the Si mirror plate are kept constant for both devices A and B. With these two different designs, we endeavor on the investigation of the effect of the number of S-shaped PZT cantilever actuator folds made on the 2-D scanning performances of the micromirror in terms of resonant frequency, optical performance and their applications.

To better understand the operation modes of both devices, finite element analysis (FEA) of the devices were performed using the ABAQUS simulation tool. The mechanical operation eigenmodes for bending and torsional modes were retrieved for both devices and the simulation results are demonstrated in Fig. 2. The color bars in Fig. 2 represent the normalization of the mode shapes according to the mass matrix. Fig. 2(a) and (b) shows the mode shapes and eigenvalues of device A for bending (34 Hz) and torsional (72 Hz) modes respectively while the mode shapes and eigenvalues for device B during bending (23 Hz) and torsional (149 Hz) modes are shown in Fig. 2(c) and (d) respectively. The eigenvalue of bending mode for device A is bigger than that of device B. This can be explained by

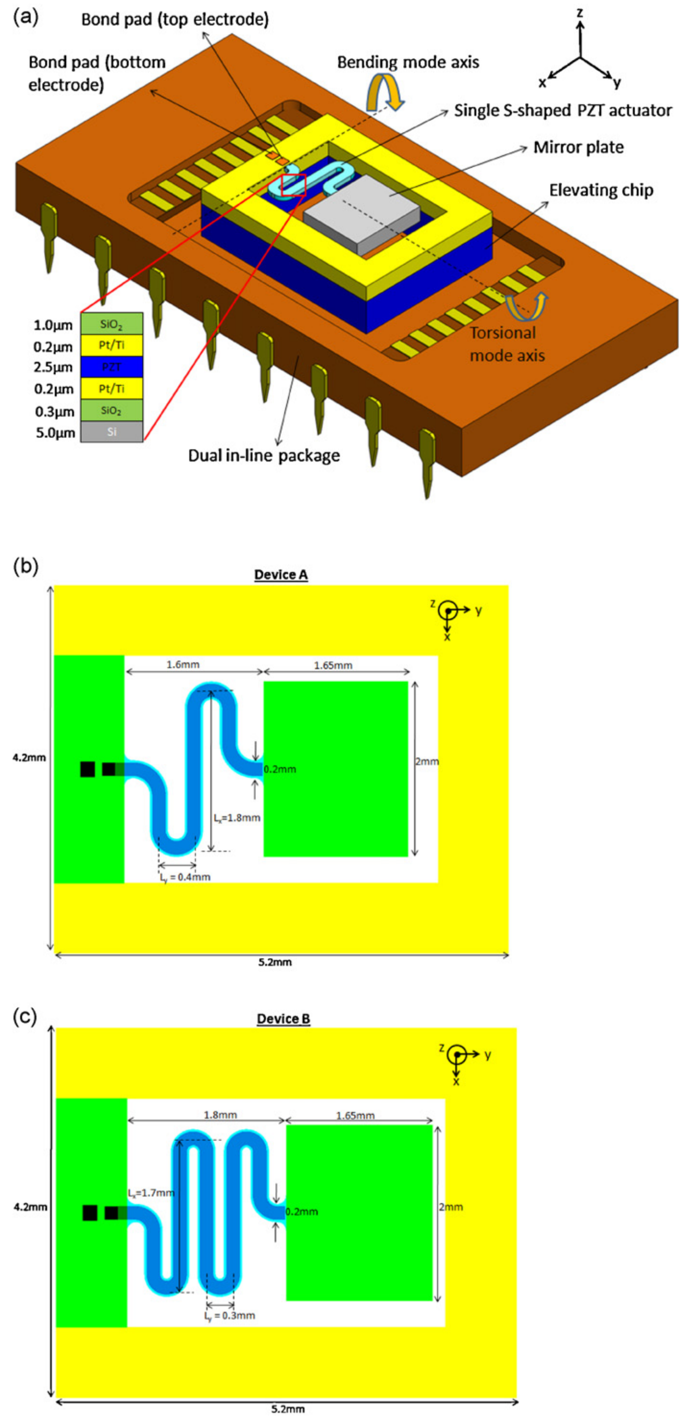

Fig. 1. (a) Schematic drawing of the packaged 2-D MEMS scanning mirror driven by a S-shaped PZT cantilever actuator where it twists or bends when ac voltages of different frequencies are applied to it. Layout drawings and dimensions of a mirror driven by a (b) single S-shaped PZT cantilever actuator, i.e. device A; (c) double S-shaped PZT actuator, i.e. device B.

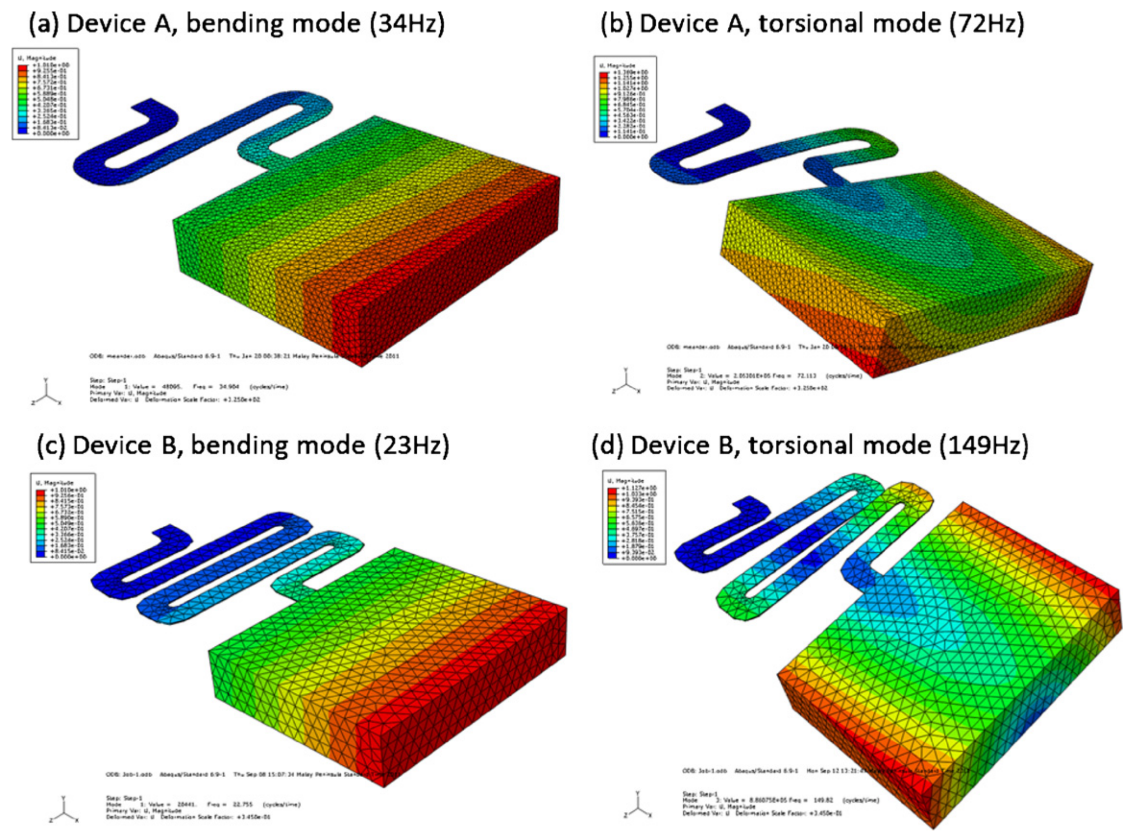

Fig. 2. Modal analysis of the two investigated designs using finite element simulation software ABAQUS. (a) Device A under bending mode, where the single S-shaped PZT cantilever actuator bends out-of-plane at a eigenvalue of 34 Hz. (b) Device A under torsional mode, where the single S-shaped PZT cantilever actuator twists out-of-plane at eigenvalue of 72 Hz. (c) Device B under bending mode, where the double S-shaped PZT cantilever actuator bends out-of-plane at eigenvalue of 23 Hz. (d) Device B under torsional mode, where the double S-shaped PZT cantilever actuator twists out-of-plane at a eigenvalue of 149 Hz.

using the equation for rotational spring constant ($K_{\theta x}$) along x-axis obtained from Ref. [46]:

$$K_{\theta x} = \left[\frac{2(N+2)}{EI}L_y + \frac{2(N+1)}{GJ}L_x\right]^{-1} \quad (1)$$

where N is the number of folds, E is Young's modulus, I is the moment of inertia with respect to the x-axis, G is the shear modulus, J is the cross-section torsion factor of the spring element parallel to the x-axis, L_x is the length of the spring element parallel to x-axis, L_y is the length of the spring element parallel to y-axis. By analyzing equation (1), it can be recognized that the first term is contributed by the bending stiffness of the spring elements (of length L_y) parallel to the y-axis, while the second term is contributed by the torsional stiffness of the elements (of length L_x) parallel to the x-axis. From (1), the ratio of $K_{\theta x}$ for device A to B can be derived as:

$$\frac{(K_{\theta x})_A}{(K_{\theta x})_B} = \frac{[2GJ(N+2)L_y + 2EI(N+1)L_x]_B}{[2GJ(N+2)L_y + 2EI(N+1)L_x]_A} \quad (2)$$

For device A, the values of N, L_x and L_y are 1, 1.8 mm and 0.4 mm respectively while for device B, the values are 2, 1.7 mm and 0.3 mm. After substituting these values of N, L_x and L_y into (2) and taking into account that the values of shear modulus (G), Young's modulus (E), moment of inertia (I) and cross-section torsion factor to be independent of L_x and L_y, a ratio of $(K_{\theta x})_A/(K_{\theta x})_B$ greater than 1 will be obtained, i.e. the rotational mechanical stiffness along x-axis for device A is greater than that of device B. This explains why the eigenvalue obtained for bending mode in Fig. 2(a) for device A is bigger compared to device B in Fig. 2(c). In the case for torsional mode, the eigenvalue obtained for device A in Fig. 2(b) is smaller than that for device B in Fig. 2(d). This is because the twisting of the mirror plate for device B happens during the 3rd eigenmode while for device A, it happens during the 2nd eigenmode.

Harmonic analysis, based on ANSYS simulation software, was also performed to investigate the ac performance of the two devices for different input frequencies. An arbitrary sinusoidal varying force was uniformly applied on the mirror plate of both devices while frequency sweep from 1 Hz to 200 Hz, with step size of 1 Hz, was made. A node at the far-right corner of the meshed mirror plate was chosen as the input point while the vertical amplitude of the node versus frequency for both designs are plotted and shown in Fig. 3. Frequency peaks at 34 Hz and 72 Hz are obtained for device A, which corresponds well to the modal analysis shown in Fig. 2(a) and (b). Similarly for device B, frequency peaks at 23 Hz and 149 Hz are obtained. In both devices, the vertical amplitudes of the vibrating mirror plate are larger during bending mode compared to torsional mode of the same device. In addition, by comparing the bending modes of the two devices, the vertical amplitude obtained for device B is smaller than that for device A. By considering the balance of the weight, i.e. the downward gravitational force acting on the mirror plate and the parallel acting restoring force of the deformed S-shaped spring actuator, the weight of the mirror will have a greater damping effect for the softer spring actuator design in device B compared to device A. This reduces the amount of energy being coupled from the biased PZT actuator to the mirror plate. As such, this may cause more energy to be lost in device B compared to device A, resulting in the vibration peak to be smaller for device B compared to device A. This trend also applies when comparing the torsional modes of both devices.

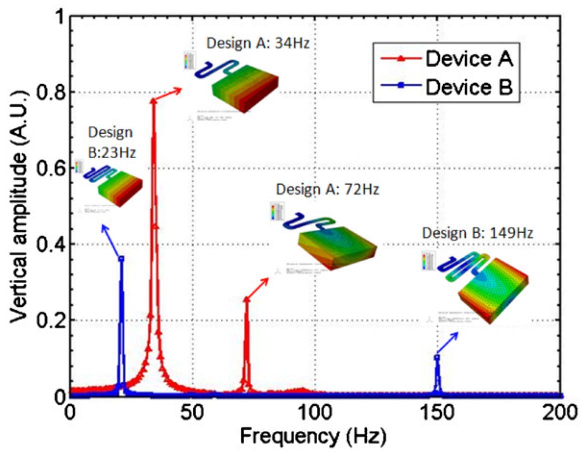

Fig. 3. Simulated plot of vertical amplitude for corner of mirror plate against frequency sweep from 1 Hz to 200 Hz, with a step size of 1 Hz obtained during harmonic analysis of the two investigated designs. An arbitrary sinusoidal varying force is uniformly applied on the mirror.

In order to evaluate and compare the dc static responses for the two devices, a mathematical model based on the following equations are used [47]:

$$\delta_{\text{cantilever}} = \frac{3\text{AB}}{K} L_{\text{longitudinal}}{}^{2} V d_{31} \tag{3}$$

$$\text{A} = S_{\text{Si}} S_{\text{PZT}} (S_{\text{PZT}} t_{\text{Si}} + S_{\text{Si}} t_{\text{PZT}}) \tag{4}$$

$$\text{B} = \frac{t_{\text{Si}}(t_{\text{Si}} + t_{\text{PZT}})}{S_{\text{PZT}} t_{\text{Si}} + S_{\text{Si}} t_{\text{PZT}}} \tag{5}$$

$$K = (S_{\text{si}})^2 (t_{\text{PZT}})^4 + 4 S_{\text{Si}} S_{\text{PZT}} t_{\text{Si}} (t_{\text{PZT}})^3 + 6 S_{\text{Si}} S_{\text{PZT}} (t_{\text{Si}})^2 (t_{\text{PZT}}) + 4 S_{\text{Si}} S_{\text{PZT}} (t_{\text{Si}})^3 (t_{\text{PZT}}) + (S_{\text{PZT}}{}^2)(t_{\text{Si}}) \tag{6}$$

where $\delta_{\text{cantilever}}$ is the displacement of the PZT actuator tip, $L_{\text{longitudinal}}$ is the length of the PZT actuator along the y-direction, V is the applied voltage, S_{Si} and S_{PZT} are the compliances of the strutural Si layer and PZT thin film respectively, t_{Si} and t_{PZT} are the respective thicknesses of the strutural silicon and PZT film and d_{31} is the piezoelectric strain constant. From (3), it can be interpreted that a longer longitudinal PZT cantilever actuator will result in a larger displacement. As such, we deliberately designed the longitudinal PZT cantilever actuator length for device B to be slightly longer than that of device A. With this minor design tweak, it will allow us to determine which factor, i.e. number of actuator folds or the longitudinal length plays a more significant role in the mirror optical performance.

3. Device microfabrication

The microfabrication process flow for the MEMS mirror is schematically depicted in Fig. 4. The process began in Fig. 4(a) with Pt/Ti/PZT/Pt/SiO_2 multilayer deposition on silicon-on-insulator (SOI) wafers with 5 μm thick Si device layer. The SOI wafers were first oxidized at 1100 °C to form a thermal oxide layer (1 μm). After the oxidation process step, Pt(0.2 μm)/Ti(0.05 μm) thin films were deposited as bottom electrode materials by dc magnetron sputtering. 2.5 μm thick $Pb(Zr_{0.52}Ti_{0.48})O_3$ (PZT) thin films of (1 0 0)-orientation were then formed by sol-gel deposition. Such (1 0 0) crystallographic orientation of PZT gives a larger piezoelectric constant compared with (1 1 1) orientated ones [48]. Finally, Pt(0.2 μm)/Ti(0.05 μm) thin films were deposited by dc magnetron sputtering. The obtained multilayers were then patterned and etched by both dry and wet methods in Fig. 4(b). The top and bottom electrodes of Pt/Ti were defined using masks 1 and 3 respectively. The electrode material was etched using Ar ions after lithography. The piezoelectric PZT film was defined using mask 2 and wet etched using a mixture of HF, HNO_3 and HCl. In Fig. 4(c), an insulating oxide layer (0.8 μm) was deposited by RF-magnetron sputtering, followed by contact hole definition through mask 4 and etched by reactive ion etching (RIE) with CHF_3 gas. In Fig. 4(d), contact hole formation using 1 μm Pt metal lines with Ti adhesion layer was done. The contact metal was deposited by sputtering, patterned and etched using mask 5 and Ar ions respectively. Through mask 6 in Fig. 4(e), the thermal oxide, Si device and BOX layers were etched by RIE using SF_6 (for Si) and CHF_3 (for SiO_2) gases. Finally, in Fig. 4(f), the Si handle layer was etched from the backside using DRIE, releasing the actuator and mirror.

After the microfabrication process, the mirror chips were assembled on a dual in-line package (DIP) as shown in Fig. 5. Elevating spacer chips of 1200 μm thickness were placed between the base of the package and the devices so as to prevent hindrance to the mirror movement during dc and ac actuations. Fig. 6(a)–(d) shows optical microscope images of the PZT cantilever actuators for devices A and B respectively. The top and bottom bond pads are connected to the pins of the DIP by gold bond wires.

The material characterization of the PZT thin film fabricated has already been investigated previously in Ref. [49]. Our non-buffered PZT thin film have (1 0 0)/(0 0 1) preferred orientation, a remnant polarization and dielectric constant of 10.5 μC cm^{-2} and 950 respectively. The transverse piezoelectric constant d_{31} measured at 30 V_{dc} is −60 pm V^{-1}.

4. Experimental setup

The experimental setup shown in Fig. 7 is used to investigate the dc and ac characteristics of the fabricated devices. The device was mounted upright perpendicular to the optical table surface on a L-shaped stand and fixed to an adjustable X–Y–Z stage. This setup is different from the one we used in our previous research attempt in Ref. [45] where the device is placed parallel to the table surface. In this setup, a red laser beam of 633 nm wavelength was impinged along the optical table surface onto the micromirror and reflected to a white screen. The screen was placed and fixed perpendicularly to the reflected light when the device was initially unbiased. The optical deflection angle (2θ) can be directly determined from the scale reading on the screen (L) and the distance of the screen from the mirror (H). A dc power supply was used for dc response experiments. In ac response experiments, two function generators, each responsible for bending and torsional modes respectively, were input into a summing amplifier (MC1741C, Motorola) to bias and excite the PZT cantilever actuator. Function generators 1 and 2 are responsible for bending and torsional modes, producing ac sinusoidal voltages of V_B and V_T respectively. Unlike our previous approaches in Refs. [43,44] where two ac signals are applied separately to two different sets of actuators to achieve 2-D scanning patterns, a summing amplifier is needed for our devices in this study so as to superimpose both ac signals into one and excite the PZT cantilever actuator. The resistors' values R_1, R_2 and R_f were chosen such that the summing amplifier achieved unity gain, i.e. the voltage applied to the device is equivalent to the summation of the input voltages from the two function generators.

Polarization process was done before the characterization of the devices as this aligns the ferroelectric domain orientation of the PZT crystals, hence enhancing the piezoelectric performance of the PZT cantilever actuator. A 20 V poling voltage, corresponding to a polarized electric field of 80 kV/cm, was applied to the PZT film for 5 min at room temperature.

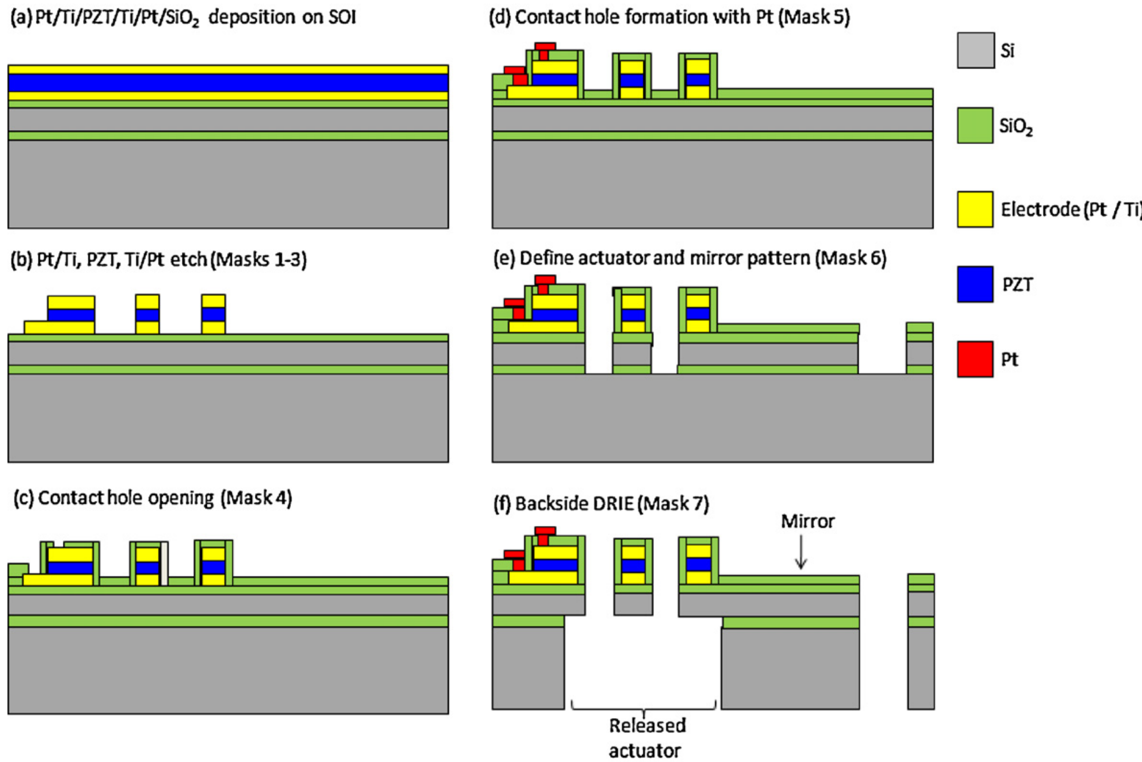

Fig. 4. Microfabrication process flow for making the S-shaped PZT cantilever actuator and the mirror.

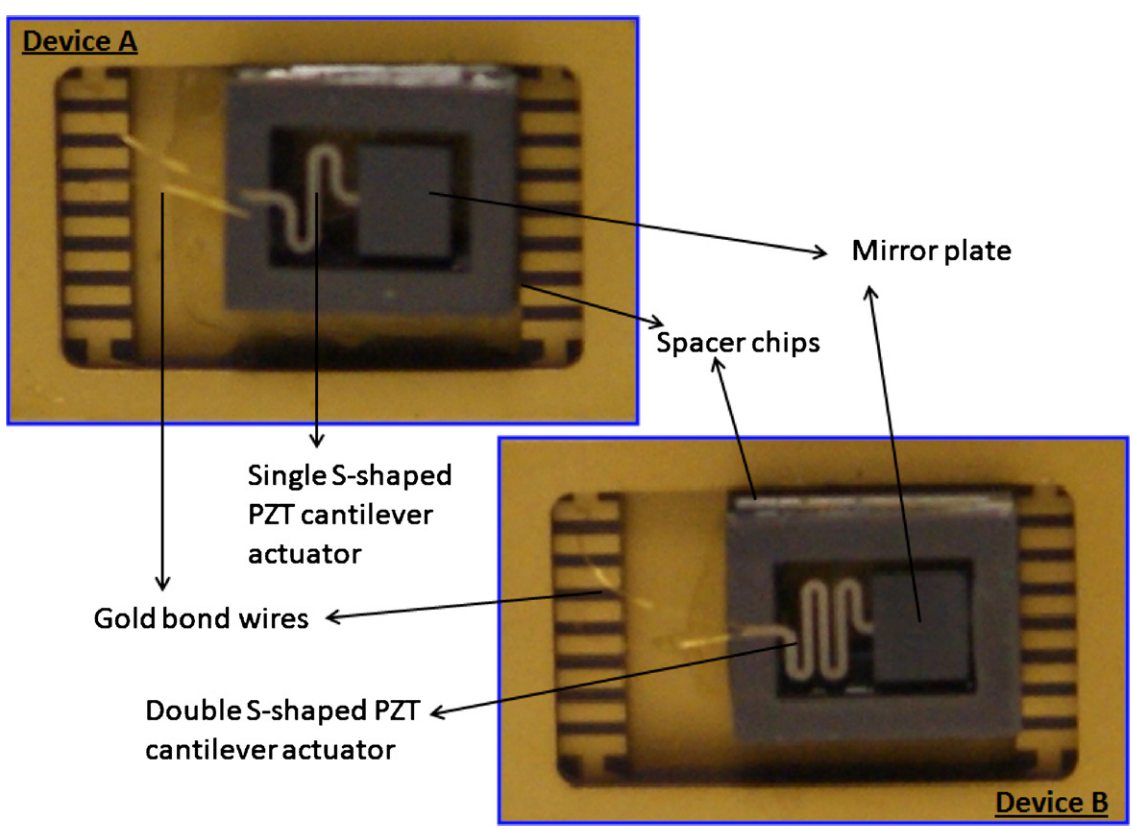

Fig. 5. Photos of the packaged MEMS mirror for devices A and B, driven by single and double S-shaped piezoelectric PZT cantilever actuator respectively.

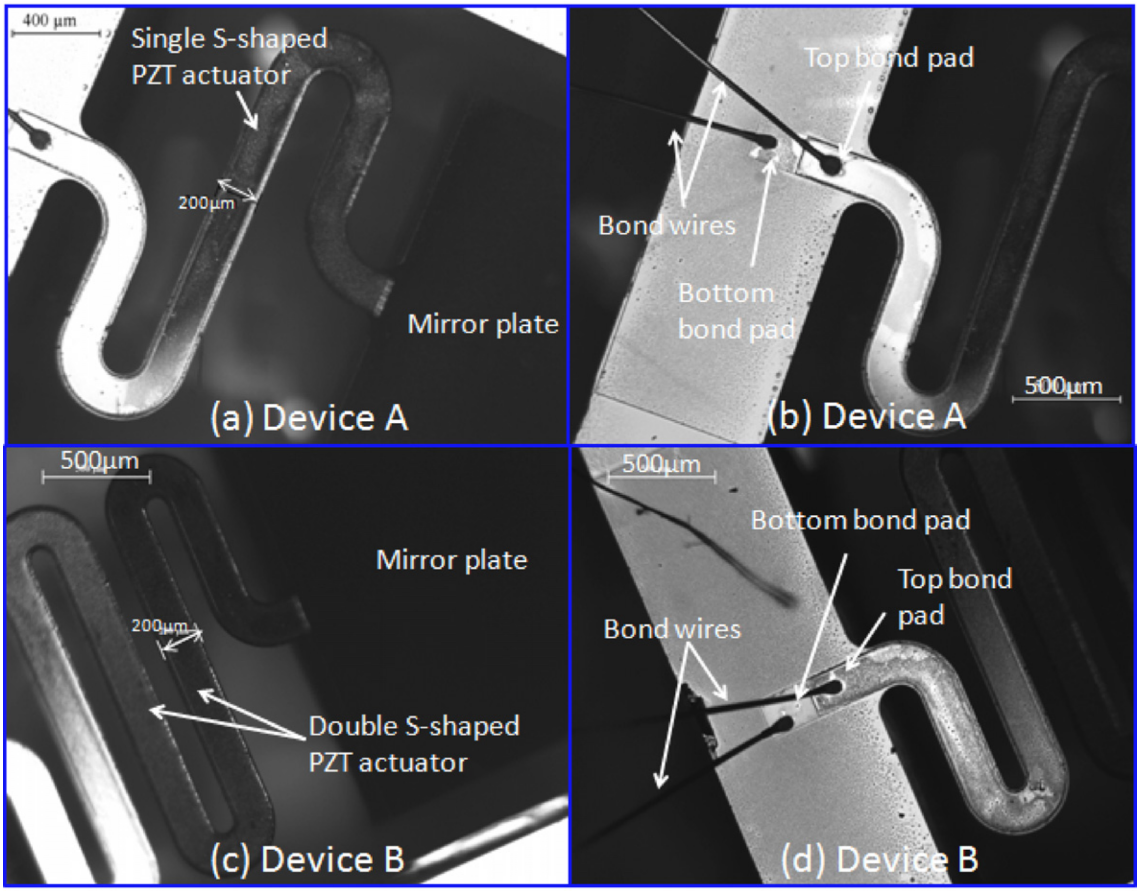

Fig. 6. Optical microscope images of (a) single S-shaped PZT actuator and a portion of the mirror plate; (b) top and bottom bond pads of device A with bond wires; (c) double S-shaped PZT actuator and a mirror plate; (d) top and bottom bond pads of device B with bond wires.

5. Results and discussion

5.1. dc response

The static response of devices A and B under unipolar dc driving voltage is shown in Fig. 8. Upon bias, the mirror translates and rotates about the *x*-axis, causing the laser spot on the screen to be displaced from its original position. This displacement is measured by a scale on the screen and the optical deflection angle (2θ) is calculated. Static optical deflection angles (ODA) of 4.6° and 3.3° are obtained at 10 V_{dc} for devices A and B respectively. More importantly, the static ODA of device A is greater than that of device B for all range of dc driving voltage investigated despite device A having a slightly shorter longitudinal PZT actuator compared to device B. This experimental result contradicts with the deduction derived from (3), whereby a longer longitudinal PZT cantilever length will result in a larger displacement. This contradiction is due to Eq. (3) being derived and valid only for simple, fixed-free rigid straight cantilever actuator structure without any meandering folds. When meandering folds are introduced to a straight cantilever structure, other factors such as the mechanical stiffness of the actuator starts to play a more important role in the actuation performance compared to the length of the actuator. The meandering folds reduces the mechanical stiffness of our investigated double S-shaped PZT cantilever actuator significantly, causing the amount of effective force that translates to displacement of the actuator to decrease. This reduces the amount of energy being coupled from the PZT actuator to the mirror plate. This observation also confirms that the number of folds in the S-shaped PZT actuator plays a more significant role on the bending actuation of the mirror compared to the longitudinal length of the actuator.

5.2. Frequency response

The frequency responses of both devices were measured in atmospheric condition and illustrated in Fig. 9. Sinusoidal ac voltage of 0.5 V_{pp}, along with a frequency sweep from 1 Hz to 1 kHz, was applied separately to both devices using a function generator. The length of the laser scanning trajectory on the screen was measured and used in the calculation of the dynamic ODA ($\pm 2\theta$). Fig. 9(a) shows the semi-log frequency spectra observed for both devices during bending mode. Primary and secondary ODA peaks of ±4.1° and ±1.6° are observed at 27 Hz and 230 Hz for device A while only one peak of ±3.5° is observed at 20 Hz for device B. The inset illustrates an example of the horizontal laser scan trajectory obtained for device A during resonant condition. The experimental resonant frequency obtained for device A is larger than that for device B. This is in agreement with our conclusion drawn from (2) as a larger spring constant ($K_{\theta x}$) for the single S-shaped actuator will lead to a larger resonant frequency during bending mode operation.

Fig. 9(b) shows the semi-log frequency spectra observed for both devices during torsional mode. Dynamic ODA peaks of ±1.1° and ±0.9° are observed at 70 Hz and 156 Hz for device A and B respectively. The observation that device B has a larger resonant frequency over device A during torsional mode implies that the rotational spring constant along *y*-axis ($K_{\theta y}$) of the double S-shaped PZT cantilever actuator is larger than that of the single S-shaped PZT

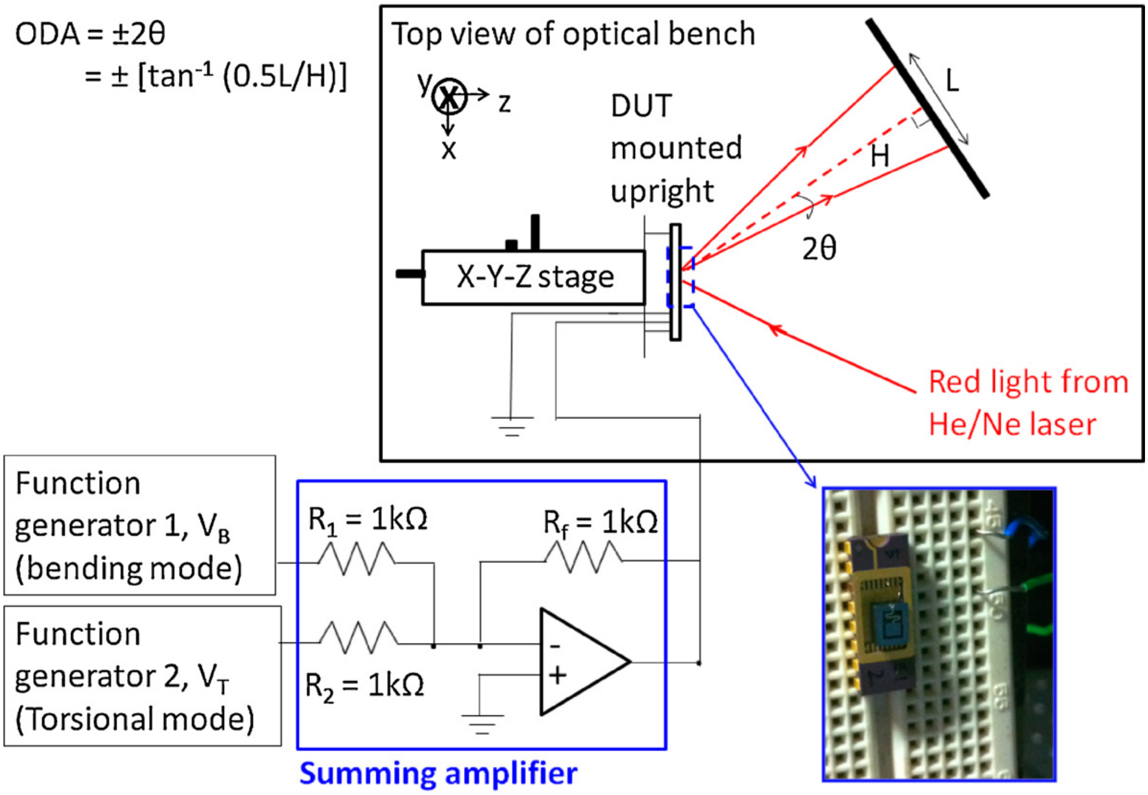

Fig. 7. Experimental setup for measuring the mirror optical deflection angle when the device is driven under dc or ac actuation voltage. A dc power supply was used for dc response experiments while two function generators, each responsible for bending and torsional modes respectively, were input into a summing amplifier to bias and excite the PZT cantilever actuator during ac response experiments. Function generator 1 is responsible for bending mode excitation and produces an ac voltage of V_B. Function generator 2 is responsible for torsional mode excitation and produces an ac voltage of V_T.

actuator. An example of the image for the vertical laser scan trajectory obtained for device A during torsional mode is depicted in the inset of Fig. 9(b). From these frequency response results, it is clear that device B, which has a greater number of S-shaped folds than device A, produces a higher ratio of frequencies of the two modes. Such design makes it favorable for 2-D scanning applications such as projection display, where a high frequency ratio between the horizontal to vertical axes is necessary for high-resolution display format [50]. However, inferior optical scanning performance remains a tradeoff inherent in the design for device B.

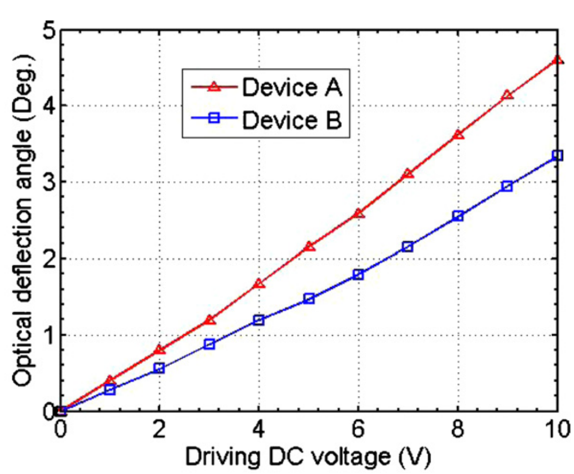

Fig. 8. Measured optical deflection angle versus driving dc voltage applied to PZT actuator for devices A and B respectively.

The comparison of the frequency values obtained from the harmonic analysis of FEA simulation and experiments are summarized in Table 1. The simulated eigenvalues obtained from the finite element harmonic analysis in Fig. 3 agree reasonably well with the experimental resonant frequencies in Fig. 9, with the small discrepancy arising due to deviation caused by lithography and fabrication. In addition, by comparing the experimental optical performance obtained during bending and torsional modes of the same device, it can be seen that a larger ODA is obtained during bending mode when compared to torsional mode. For example, ratios of 3.7 and 3.9 are obtained for devices A and B respectively when comparing the experimental ODA obtained during bending mode to torsional mode. This coincides rather closely with the simulated amplitude ratios of 3.0 obtained during harmonic analysis for both devices. It is also noted that device A performs better, in terms of ODA, for both modes when compared to device B. Both of these experimental trends echo well with the simulation trends we observed previously from Fig. 3.

5.3. ac response

The ac response during bending and torsional modes for both the devices are subsequently investigated and shown in Fig. 10.

Table 1
Comparison of frequency values obtained from simulations and experiments.

	Bending mode		Torsional mode	
	FEA simulation	Experimental	FEA simulation	Experimental
Device A	34 Hz	27 Hz	72 Hz	70 Hz
Device B	23 Hz	20 Hz	149 Hz	156 Hz

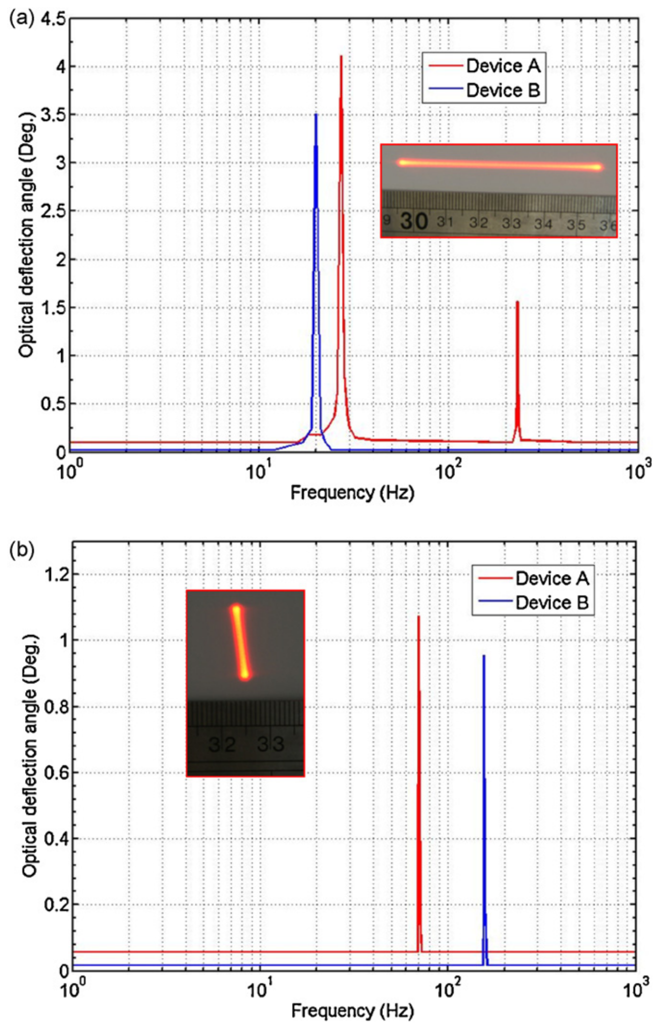

Fig. 9. Semi-log spectra of optical deflection angle versus ac sinusoidal actuation frequencies at 0.5 V_{pp} for devices A and B during (a) bending mode; (b) torsional mode, with the insets showing the scanning trajectories obtained during the two modes.

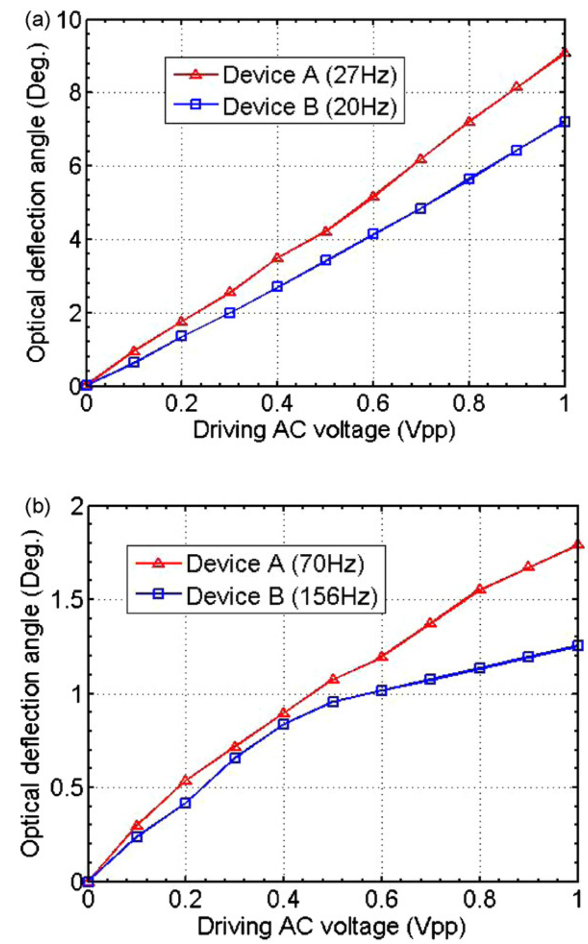

Fig. 10. Measured optical deflection angle versus driving ac voltages for devices A and B during (a) bending mode and (b) torsional mode.

In Fig. 10(a), both devices were excited at their respective resonant frequency for bending mode while sinusoidal driving voltage sweep up to 1 V_{pp} was made. For the same ac driving voltage, device A achieved a larger dynamic ODA compared to device B. For example, at 1 V_{pp}, device A achieved $\pm 9.1^{\circ}$ at resonant frequency of 27 Hz while device B achieved $\pm 7.2^{\circ}$ at 20 Hz. This observation concurs with that of dc response, i.e. device A performs larger deflection angle compared to device B in both dc and ac excitation. In addition, the dynamic ODA of $\pm 9.1^{\circ}$ obtained at 1 V_{pp} is significantly larger when compared to the static ODA of 0.4° obtained at 1 V_{dc}. This phenomenon is due to the device attaining mechanical resonance behavior from the ac electrical excitation, resulting in maximum energy transfer from the ac electrical signal to the vibrating mechanical structures.

For torsional mode ac response experiment in Fig. 10(b), the biasing setup is similar to that for bending mode except that devices A and B were excited at 70 Hz and 156 Hz respectively. At 1 V_{pp}, device A obtained a dynamic ODA of $\pm 1.8^{\circ}$ while device B obtained a smaller ODA of $\pm 1.2^{\circ}$. This difference in the actuation performance between the two devices can be explained by the rotational spring constant along y-axis ($K_{\theta y}$) of the double S-shaped PZT cantilever actuator being larger than that of the single S-shaped PZT actuator. In addition, for the same ac actuation voltage, the ODA during bending mode is much larger than that for torsional mode. This is because in bending mode, the mirror undergoes both translational and rotational motion in the x-axis whereas in torsional mode, the mirror only rotates about the y-axis. Such rotational movement of the mirror plate during torsional mode would not induce displacement of the laser reflection path as much as bending mode do, hence making bending mode more effective in beam steering.

In both modes, it is noted that the difference in performances between both the devices during bending and torsional modes become smaller for the experimental results as compared to the harmonic simulation result obtained in Fig. 3. This is due to the device being mounted upright in the experimental setup shown in Fig. 7. As a result, the downward gravitational force acting on the mirror has reduced effect on the performance of the device as the direction of swing of the mirror plate is perpendicular to the gravitational force at equilibrium position. However, the gravitational force vector changes with respect to the various positions of a single vibration swing. When the mirror rotation angle becomes significant, the damping effect brought about by the gravitational force vector increases at the boundary of a vibration swing. Thus, the scanning angle difference between devices A and B becomes larger under a higher ac driving voltage for both modes.

5.4. Mixed mode operation

In mixed mode operation, frequencies corresponding to the bending and torsional modes are input into the summing amplifier simultaneously to excite the devices. To prove the effect of the summing amplifier on the two input ac signals from the function

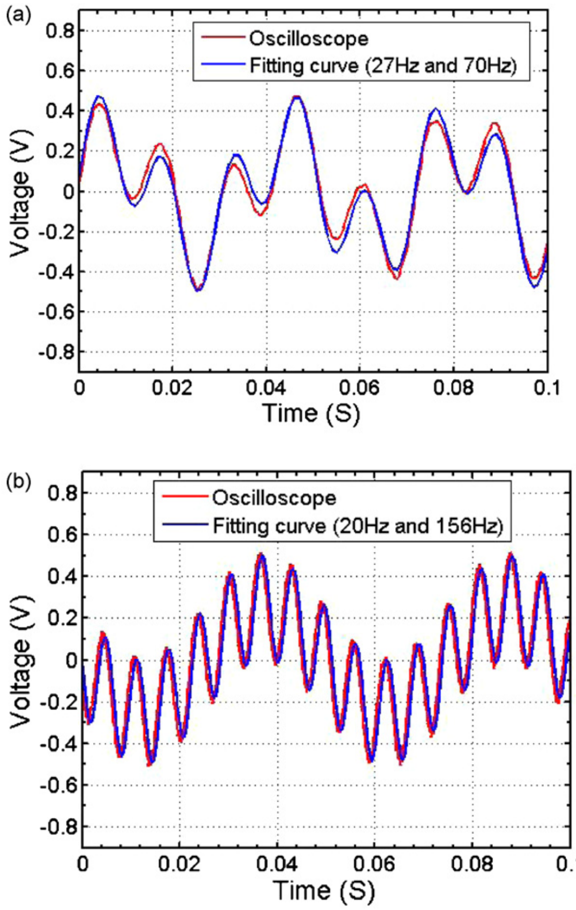

Fig. 11. Waveform obtained from the oscilloscope during mixed mode operation and derived from the fitting curves respectively for (a) device A and (b) device B.

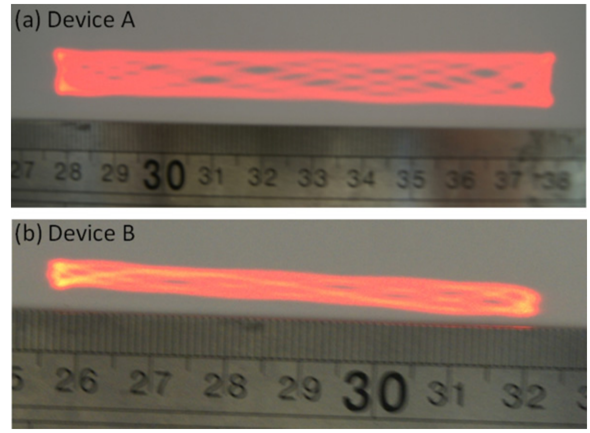

Fig. 12. Lissajous scan pattern obtained in resonance during mixed mode operation with (a) device A and (b) device B.

generators, an oscilloscope was placed at the output of the summing amplifier to detect the signal. The red graph in Fig. 11(a) shows the signals detected by the oscilloscope when the frequency inputs by function generators 1 and 2 used to excite device A are 0.5 V_{pp}, 27 Hz and 0.5 V_{pp}, 70 Hz respectively. The blue graph in Fig. 10(a) shows the fitting curve, which is mathematically represented by:

$$V_{out} = -[0.25\ \sin[\omega_B(t + t_1)] + 0.25 \sin[\omega_T(t + t_1)]] \quad (7)$$

where $\omega_B = 2\pi(27)$, $\omega_T = 2\pi(70)$, and t_1 is the amount of time shift needed to match the curve to the oscilloscope trace. The close fitting of the blue curve with the red curve confirms that the superimposed output signal from the summing amplifier is equivalent to the summation of the two input sinusoidal signals by the function generators. The close fitting of both the blue and the red curves is also observed for device B and reflected in Fig. 11(b). Such experimental confirmation is important as it allows us to ensure that the output superimposed signal from the summing amplifier retains the ac characteristics of the input signals from the function generators and remains controllable through the adjustment of the various parameters such as V_B, V_T and frequencies.

Fig. 12 illustrates the 2-D Lissajous scan pattern obtained in resonance during mixed mode operation for both devices. An example of the scan pattern for device A is demonstrated in Fig. 12(a) while similar 2-D resonance Lissajous scan pattern is obtained in Fig. 12(b) for device B when it is driven at the respective resonant frequency for both bending and torsional modes. To achieve better optical performance in terms of larger ODA and resonant frequencies, various optimizations may be made for both our designs. For example, the sol-gel deposition process for the PZT thin film can be refined further as PZT films with very large piezoelectric strain constant of 260 pm V^{-1} have already been reported [51]. In addition, the mirror size can be reduced so that the mass is reduced and the resonance frequency can be extended to the kilohertz range.

6. Conclusion

A novel 2-D MEMS scanning mirror driven by simultaneous dynamic excitation of two different modes on an S-shaped piezoelectric PZT actuator is explored. Two different PZT actuator designs have been fabricated and characterized. With these two different designs, investigation on the effects of the dimensions and number of S-shaped PZT cantilever actuator folds on the 2-D scanning performances of the micromirror have been made. An experimental setup which involved the devices being mounted upright perpendicular to the optical table surface was performed to reduce the effect of gravity on the performance of the devices. Device A, which is driven by single S-shaped PZT cantilever actuator, performs better in both dc and ac laser scanning compared to the double S-shaped PZT actuator driven device B. The differences in scanning angles between devices A and B become larger under higher dc and ac driving voltages. This is due to increase damping effect brought about by the increased gravitational force vector acting on the mirror plate for device B compared to device A. In terms of frequency response, a larger frequency ratio between the horizontal to vertical axes is observed for device B (∼8) compared to device A (∼2.6). Such double S-shaped actuator design for device B makes it favorable for 2-D scanning applications such as projection display, where a high frequency ratio between the horizontal to vertical axes is necessary for high-resolution display format. However, inferior optical scanning performance remains a tradeoff inherent in device B. Last but not least, Lissajous scan patterns have been successfully demonstrated by both devices, hence demonstrating their potential in 2-D imaging applications.

Acknowledgements

The authors would like to acknowledge the support by the National University of Singapore under Grant No. R-263-000-475-112, MOE2009-T2-2-011 (R-263-000-598-112), SERC Grant No. 1021010022 and 1021650084 from A*STAR, Singapore and the Ph.D. scholarship grant received from GlobalFoundries Singapore.

References

[1] C. Lee, J.A. Yeh, Development and evolution of MOEMS technology in variable optical attenuators, Journal of Micro/Nanolithography, MEMS, and MOEMS 7 (2008) 021003.
[2] C. Lee, F.-L. Hsiao, T. Kobayashi, K.H. Koh, P.V. Ramana, W. Xiang, B. Yang, C.W. Tan, D. Pinjala, A 1-V operated MEMS variable optical attenuator using piezoelectric PZT thin-film actuators, IEEE Journal of Selected Topics in Quantum Electronics 15 (2009) 1529–1536.
[3] K.H. Koh, C. Lee, T. Kobayashi, A piezoelectric-driven three-dimensional MEMS VOA using attenuation mechanism with combination of rotational and translational effects, IEEE/ASME Journal of Microelectromechanical Systems 19 (2010) 1370–1379.
[4] J.A. Yeh, S.-S. Jiang, C. Lee, MOEMS variable optical attenuators using rotary comb drive actuators, IEEE Photonics Technology Letters 18 (2006) 1170–1172.
[5] R.F. Wolffenbuttel, MEMS-based optical mini- and microspectrometers for the visible and infrared spectral range, Journal of Micromechanics and Microengineering 15 (2005) S145–S152.
[6] J.S. Milne, J.M. Dell, A.J. Keating, L. Faraone, Widely tunable mems-based Fabry Perot filter, IEEE/ASME Journal of Microelectromechanical Systems 18 (2009) 905–913.
[7] N. Neumann, M. Ebermann, S. Kurth, K. Hiller, Tunable infrared detector with integrated micromachined Fabry-Perot filter, Journal of Micro/Nanolithography, MEMS, and MOEMS 7 (2008) 021004.
[8] J.J. Sun, S.G. Guo, L. Wu, L. Liu, S.W. Choe, B.S. Sorg, H. Xie, 3D in vivo optical coherence tomography based on a low-voltage, large-scan-range 2D MEMS mirror, Optics Express 18 (2010) 12065–12075.
[9] Y. Wang, M. Raj, H.S. McGuff, G. Bhave, B. Yang, T. Shen, X. Zhang, Portable oral cancer detection using a miniature confocal imaging probe with a large field of view, Journal of Micromechanics and Microengineering 22 (2012) 065001.
[10] Y. Xu, J. Singh, C.S. Premachandran, A. Khairyanto, K.W.S. Chen, N. Chen, C.J.R. Sheppard, M. Olivo, Design and development of a 3D scanning MEMS OCT probe using a novel SiOB package assembly, Journal of Micromechanics and Microengineering 18 (2008) 125005.
[11] A.D. Aguirre, P.R. Herz, Y. Chen, J.G. Fujimoto, W. Piyawattanametha, L. Fan, M.C. Wu, Two-axis MEMS scanning catheter for ultrahigh resolution three-dimensional and en face imaging, Optics Express 15 (2007) 2445–2453.
[12] C.-D. Liao, J.-C. Tsai, The evolution of MEMS displays, IEEE Transactions on Industrial Electronics 56 (2009) 1057–1065.
[13] A.D. Yalcinkaya, H. Urey, D. Brown, T. Montague, R. Sprague, Two-axis electromagnetic microscanner for high resolution displays, IEEE/ASME Journal of Microelectromechanical Systems 15 (2006) 786–794.
[14] K.H. Koh, C. Lee, A two-dimensional MEMS scanning mirror using hybrid actuation mechanisms with low operation voltage, IEEE/ASME Journal of Microelectromechanical Systems (2012), http://dx.doi.org/10.1109/JMEMS.2012.2196497.
[15] T. Kobayashi, R. Maeda, T. Itoh, R. Sawada, Smart optical microscanner with piezoelectric resonator, sensor, and tuner using $Pb(Zr,Ti)O_3$ thin film, Applied Physics Letters 90 (2007) 183514.
[16] Y. Du, G. Zhou, K.L. Cheo, Q. Zhang, H. Feng, F.S. Chau, Double-layered vibratory grating scanners for high-speed high-resolution laser scanning, IEEE/ASME Journal of Microelectromechanical Systems 19 (2010) 1186–1196.
[17] Y. Du, G. Zhou, K.K.L. Cheo, Q. Zhang, H. Feng, F.S. Chau, A 21.5 kHz high optical resolution electrostatic double-layered vibratory grating laser scanning, Sensors and Actuators A: Physical 168 (2011) 253–261.
[18] B.E. Yoxall, R. Walmsley, H.-P. Kuo, S.-Y. Wang, T.M.D.A. Horsley, Two-axis MEMS lens alignment system for free-space optical interconnect, IEEE Journal of Selected Topics in Quantum Electronics 17 (2011) 559–565.
[19] H.C. Park, C. Song, K.H. Jeong, Micromachined lens microstages for two-dimensional forward optical scanning, Optics Express 18 (2010) 16133–16138.
[20] L. Wu, H. Xie, A millimeter-tunable-range microlens for endoscopic biomedical imaging applications, IEEE Journal of Selected Topics in Quantum Electronics 46 (2010) 1237–1244.
[21] J. Lincoln, The latest video projectors can fit inside tiny cameras or cellphones yet still produce big pictures [Little Gizmo, Big Picture], IEEE Spectrum 47 (2010) 41–45.
[22] G.K. Fedder, R.T. Howe, L. Tsu-Jae King, E.P. Quevy, Technologies for cofabricating MEMS and electronics, Proceedings of the IEEE 96 (2008) 306–322.
[23] P.J. Gilgunn, J. Liu, N. Sarkar, G.K. Fedder, CMOS-MEMS lateral electrothermal actuators, IEEE/ASME Journal of Microelectromechanical Systems 17 (2008) 103–114.
[24] H. Xie, Y. Pan, G.K. Fedder, A CMOS-MEMS mirror with curled-hinge comb drives, IEEE/ASME Journal of Microelectromechanical Systems 12 (2003) 450–457.
[25] J.L.A. Yeh, H. Jiang, N.C. Tien, Integrated polysilicon and DRIE bulk silicon micromachining for an electrostatic torsional actuator, IEEE/ASME Journal of Microelectromechanical Systems 8 (1999) 456–465.
[26] R. Maeda, J.J. Tsaur, S.H. Lee, M. Ichiki, Piezoelectric microactuator devices, Journal of Electroceramics 12 (2004) 89–100.
[27] J. Baborowski, Microfabrication of piezoelectric MEMS, Integrated Ferroelectrics 66 (2004) 33–51.
[28] C. Lee, T. Itoh, T. Suga, Self-excited piezoelectric PZT microcantilevers for dynamic SFM – with inherent sensing and actuating capabilities, Sensors and Actuators A: Physical 72 (1999) 179–188.
[29] U. Baran, D. Brown, S. Holmstrom, D. Balma, W.O. Davis, A. Mazzalai, P. Muralt, H. Urey, High frequency torsional MEMS scanner for displays, in: Proc. IEEE Int. Conf. Micro Electro Mechanical Systems, Paris, France, 2012, pp. 636–639.
[30] F. Filhol, E. Defay, C. Divoux, C. Zinck, M.T. Delaye, Resonant micro-mirror excited by a thin-film piezoelectric actuator for fast optical beam scanning, Sensors and Actuators A: Physical 123–124 (2005) 483–489.
[31] J. Tsaur, Z. Lulu, R. Maeda, S. Matsumoto, 2D micro scanner actuated by sol–gel derived double layered PZT, in: 15th IEEE International Conference on Micro Electro Mechanical Systems, 2002, pp. 548–551.
[32] Y. Yasuda, M. Akamatsu, M. Tani, T. Iijima, H. Toshiyoshi, Piezoelectric 2D-optical micro scanners with PZT thick films, Integrated Ferroelectrics 76 (2005) 81–91.
[33] M. Tani, M. Akamatsu, Y. Yasuda, H. Toshiyoshi, A two-axis piezoelectric tilting micromirror with a newly developed PZT-meandering actuator, in: IEEE 20th International Conference on Micro Electro Mechanical Systems, 2007, pp. 699–702.
[34] Y. Zhu, W. Liu, K. Jia, W. Liao, H. Xie, A piezoelectric unimorph actuator based tip-tilt-piston micromirror with high fill factor and small tilt and lateral shift, Sensors and Actuators A: Physical 167 (2011) 495–501.
[35] K. Jia, S. Pal, H. Xie, An electrothermal tip-tilt-piston micromirror based on folded dual S-shaped bimorphs, IEEE/ASME Journal of Microelectromechanical Systems 18 (2009) 1004–1015.
[36] K. Jongbaeg, D. Christensen, L. Lin, Monolithic 2-D scanning mirror using self-aligned angular vertical comb drives, IEEE Photonics Technology Letters 17 (2005) 2307–2309.
[37] H.M. Chu, K. Hane, Design, fabrication and vacuum operation characteristics of two-dimensional comb-drive micro-scanner, Sensors and Actuators A: Physical 165 (2011) 422–430.
[38] T.-L. Tang, C.-P. Hsu, W.-C. Chen, W. Fang, Design and implementation of a torque-enhancement 2-axis magnetostatic SOI optical scanner, Journal of Micromechanics and Microengineering 20 (2010) 025020.
[39] C.-H. Ji, M. Choi, S.-C. Kim, K.-C. Song, J.-U. Bu, H.-J. Nam, Electromagnetic two-dimensional scanner using radial magnetic field, IEEE/ASME Journal of Microelectromechanical Systems 16 (2007) 989–996.
[40] H.-A. Yang, T.-L. Tang, S.T. Lee, W. Fang, A novel coilless scanning mirror using eddy current lorentz force and magnetostatic force, IEEE/ASME Journal of Microelectromechanical Systems 16 (2007) 511–520.
[41] A.D. Yalcinkaya, H. Urey, S. Holmstrom, NiFe plated biaxial MEMS scanner for 2-D imaging, IEEE Photonics Technology Letters 19 (2007) 330–332.
[42] S.O. Isikman, O. Ergeneman, A.D. Yalcinkaya, H. Urey, Modeling and characterization of soft magnetic film actuated 2-D scanners, IEEE Journal of Selected Topics in Quantum Electronics 13 (2007) 283–289.
[43] K.H. Koh, T. Kobayashi, F.-L. Hsiao, C. Lee, Characterization of piezoelectric PZT beam actuators for driving 2D scanning micromirrors, Sensors and Actuators A: Physical 162 (2010) 336–347.
[44] K.H. Koh, T. Kobayashi, J. Xie, A. Yu, C. Lee, Novel piezoelectric actuation mechanism for a gimbal-less mirror in 2D raster scanning applications, Journal of Micromechanics and Microengineering 21 (2011) 075001.
[45] K.H. Koh, T. Kobayashi, C. Lee, A 2-D MEMS scanning mirror based on dynamic mixed mode excitation of a piezoelectric PZT thin film S-shaped actuator, Optics Express 19 (2011) 13812–13824.
[46] G. Barillaro, A. Molfese, A. Nannini, F. Pieri, Analysis, simulation and relative performances of two kinds of serpentine springs, Journal of Micromechanics and Microengineering 15 (2005) 736.
[47] J.G. Smits, W. Choi, The constituent equations of piezoelectric heterogeneous bimorphs, IEEE Transactions on Ultrasonics, Ferroelectrics and Frequency Control 38 (1991) 256–270.
[48] D. Taylor, D. Damjanovic, Piezoelectric properties of rhombohedral $Pb(Zr,Ti)O_3$ thin films with (1 0 0), (1 1 1), and "random" crystallographic orientation, Applied Physics Letters 76 (2000) 1615.
[49] T. Kobayashi, M. Ichiki, R. Kondou, K. Nakamura, R. Maeda, Fabrication of piezoelectric microcantilevers using $LaNiO_3$ buffered $Pb(Zr,Ti)O_3$ thin film, Journal of Micromechanics and Microengineering 18 (2008) 35007-031–35007-035.
[50] H. Urey, D. Wine, T. Osborn, Optical performance requirements for MEMS-scanner-based microdisplays, Proceedings of the SPIE 4178 (2000) 176.
[51] P. Muralt, R.G. Polcawich, S. Trolier-McKinstry, Piezoelectric thin films for sensors, actuators, and energy harvestin, MRS Bulletin 34 (2009) 658–664.

Biographies

Kah How Koh received his B.Eng. (Hons) degree from the Department of Electrical and Computer Engineering, National University of Singapore (NUS), Singapore, in 2009. He is currently working toward the Ph.D. degree in electrical engineering with NUS. His research work is on the development of novel actuation mechanisms for optical microelectromechanical systems, focusing mainly on 2-D scanning and variable optical attenuation applications. He has since contributed 18 peer-reviewed international journal and conference articles in the capacity of first author. Mr. Koh was the recipient of Singapore Economic Development Board (EDB)-GlobalFoundries Graduate Scholarship for 2009–2013. He was also the recipient of three Best Student Paper Awards for IEEE Photonics Global Conference 2010, 16th and 17th Opto-Electronics and Communications Conference (OECC 2011 & OECC 2012), respectively.

Takeshi Kobayashi received his B.S. and M.S. degree in materials science from The University of Tokyo. He also received Ph.D. degree in materials science from The University of Tokyo in 2002. He worked as researcher in National Institute of Advance Industrial Science and Technology (AIST), Japan. His research interest includes piezoelectric MEMS devices and their application to wireless sensor network. He has contributed more than 70 international journal papers and conference proceedings. Two of his publications have been selected as highlighted paper of Journal of Micromechanics and Microengineering in 2007 and 2008. He has also been the correspondence and involved in the organization of Symposium C-4: Green Micro Energy Management Systems of International Union of Materials Research Societies – International Conference on Electronic Materials (IUMRS-ICEM) 2012.

Chengkuo Lee received his M.S. degree in Materials Science and Engineering from National Tsing Hua University, Hsinchu, Taiwan, in 1991. He also received a M.S. degree in Industrial and System Engineering from Rutgers University, New Brunswick, NJ, USA in 1993. He received the Ph.D. degree in Precision Engineering from the University of Tokyo, Tokyo, Japan, in January 1996. He worked as foreign researcher in the Nanometer-scale Manufacturing Science Lab. at Research Center for Advanced Science and Technology (RCAST) of the University of Tokyo from 1993 to 1996. He had also worked in Mechanical Engineering Lab., AIST, MITI of Japan as a JST research fellow in 1996. Thereafter he was a senior research staff of Microsystems Lab., Industrial Technology Research Institute (ITRI), Hsinchu, Taiwan. Since September 1997, he has joined the Metrodyne Microsystem Corporation, Hsinchu, Taiwan, and established the MEMS device division and the 1st micromachining fab for commercial purpose in Taiwan. He was the manager of MEMS device division between 1997 and 2000. He had been the adjunct assistant professor in Electro-physics Department of National Chiao Tung University in 1998, and the adjunct assistant professor in Institute of Precision Eng. of National Chung Hsing University since 2001–2005. He co-founded the Asia Pacific Microsystems, Inc. (APM) Hsinchu, Taiwan, in Aug. 2001, and he has been the vice president (VP) of R&D at the beginning, then become the VP of optical communication business unit and special assistant of CEO in charge of international business and technical marketing for MEMS foundry service at APM, Inc., one of the top 30 MEMS manufacturers in the world in 2004. From 2006 to 2009, he has been a senior member of technical staff at the Institute of Microelectronics (IME), A*STAR, Singapore. He has been an assistant professor at the Dept. of Electrical and Computer Eng. of National University of Singapore, Singapore since December 2005. He is the coauthor of *Advanced MEMS Packaging* (McGraw-Hill, 2010). He has contributed more than 150 international conference papers and extended abstracts, 100 peer-reviewed international journal articles, in the fields of MEMS, nanophotonics and nanotechnology. He is also the holder of nine U.S. patents.